

Citation for published version:

Zhu, H, Wang, B, Ji, H, Soleimani, M & Jiang, Y 2024, 'A Wideband Contactless Electrical Impedance Tomography System', *IEEE Transactions on Instrumentation and Measurement*.
<https://doi.org/10.1109/TIM.2024.3351263>

DOI:

[10.1109/TIM.2024.3351263](https://doi.org/10.1109/TIM.2024.3351263)

Publication date:

2024

Document Version

Peer reviewed version

[Link to publication](#)

© 2024 IEEE. Personal use of this material is permitted. Permission from IEEE must be obtained for all other users, including reprinting/ republishing this material for advertising or promotional purposes, creating new collective works for resale or redistribution to servers or lists, or reuse of any copyrighted components of this work in other works.

University of Bath

Alternative formats

If you require this document in an alternative format, please contact:
openaccess@bath.ac.uk

General rights

Copyright and moral rights for the publications made accessible in the public portal are retained by the authors and/or other copyright owners and it is a condition of accessing publications that users recognise and abide by the legal requirements associated with these rights.

Take down policy

If you believe that this document breaches copyright please contact us providing details, and we will remove access to the work immediately and investigate your claim.

A Multifrequency Capacitively Coupled Electrical Impedance Tomography (MFCCEIT) System

Huaiyin Zhu, Baoliang Wang, Haifeng Ji, Manuchehr Soleimani and Yandan Jiang

Abstract— Objective: This work focuses on the development of a multifrequency capacitively coupled electrical impedance tomography (MFCCEIT) system with a wide bandwidth of 20 MHz. **Methods:** The MFCCEIT system consists of the 12-electrode CCEIT sensor, the sensing modules, the data acquisition module, and the personal computer (PC). The impedance calculation model is established by combining the mechanism modeling of the integrated circuits (ICs) and the empirical modeling of the measurement data with the least squares (LS) method. Experiments were carried out to evaluate the developed MFCCEIT system from the aspects of SNR, impedance measurement accuracy, and imaging performance. **Results:** Experimental results show that the system has an SNR higher than 65 dB at multiple frequencies up to 20 MHz. Impedance measurement results show that the developed system has good impedance measurement accuracy at frequencies below 10 MHz and acceptable accuracy at 10MHz - 20MHz. Imaging results of the linear back projection algorithm indicate that the MFCCEIT system has good imaging performance for both the real part and the imaginary part of the impedance at different frequencies. It can image multiple anomalies and multiple materials. **Conclusion:** The design and development of the MFCCEIT system are valid. The results verify the effectiveness of the MFCCEIT system and the impedance measurement model. **Significance:** Few types of research on the specific CCEIT system for biomedical applications have been reported. This work is the first attempt to develop an MFCCEIT system, which is of great significance for further research works.

Index Terms—Electrical impedance tomography, capacitively coupled electrical impedance tomography (CCEIT), multifrequency measurement, imaging system

I. INTRODUCTION

Electrical impedance tomography (EIT), which can noninvasively reconstruct the conductivity distribution of conductive medium, has become a promising technique in the biomedical field [1], [2], [3], [4]. It has the advantages of no radiation, low cost, and high speed. Previous studies have shown the effectiveness and potential of EIT in the imaging of the human body, such as the lung, brain, muscle, breast, and more [5]. However, the conventional EIT still cannot meet the

increasing requirements of practical applications. There exist several problems to be solved, mainly including the electrode-skin contact impedance, and the relatively low imaging quality [6].

The inaccurately known electrode-skin contact impedance has resulted from the strict contact measurement requirement of EIT, which is usually high and quite variable due to body surface condition and body movement [7], [8]. In the past decades, researchers have made considerable efforts to overcome this problem. Hua *et al.* [9] adopted an approach where the complete electrode model without any geometrical constraints was established for estimating the contact impedance. Kolehmainen *et al.* [10] proposed an image reconstruction method in which the systematic errors induced by contact impedance are eliminated as part of the image reconstruction. These ideas are based on reducing the contact impedance or establishing a complex model of contact impedance to improve the accuracy of impedance measurement. In 2013, Wang *et al.* [11] provided a different idea to overcome the problems resulting from contact measurement. By referring to the capacitively coupled contactless conductivity detection (C⁴D) technique, a new contactless alternative of EIT termed capacitively coupled electrical resistance tomography (CCERT) was proposed. Further, CCERT was extended to capacitively coupled electrical impedance tomography (CCEIT) by making full use of the impedance information, including both the real part and the imaginary part [12]. Although CCERT/CCEIT initially focuses on multiphase flow measurement in industry, it also provides a new reference for the improvement of biomedical EIT. To avoid the contact impedance problem in biomedical EIT, Jiang *et al.* [13] introduced CCEIT to biomaterial and biomedical applications. Based on phantom experiments with different biomaterials and using the impedance analyzer to implement impedance measurement acquisition, the feasibility and potential of CCEIT in biomedical imaging have been verified [14]. However, as a new technique, the research on biomedical CCEIT is still insufficient. More research is needed,

This paragraph of the first footnote will contain the date on which you submitted your paper for review. It will also contain support information, including sponsor and financial support acknowledgment. For example, "This work was supported in part by the U.S. National Science Foundation under Grant BS123456".

The next few paragraphs should contain the authors' current affiliations. Include detailed surface address and e-mail address only for the corresponding

author. For example, F. A. The author is with the National Institute of Standards and Technology, Boulder, CO, USA. S. B. Author, Jr., was with Rice University, Houston, TX, USA. He is now with Colorado State University, Fort Collins, CO, USA. *T. C. Author is with the University of Colorado, Boulder, CO, USA (correspondence e-mail: author@uoc.edu).

especially on the development of a specific CCEIT system for bio-impedance measurement/imaging.

On the other hand, the imaging quality of EIT is relatively low when compared with computed tomography (CT) or magnetic resonance imaging (MRI). Improving the imaging performance of EIT is an important research focus for researchers in the past decades. CCEIT has verified that making full use of both the real part and the imaginary part of the impedance is an effective way to improve imaging performance [15]. Besides, in recent years, researchers pay more attention to improving the imaging performance of EIT from multifrequency or spectroscopy measurement acquisition. By integrating multi-frequency impedance information, better imaging results are expected for either time-difference imaging or frequency-difference imaging [16]. Therefore, developing high-performance multifrequency EIT (MFEIT) systems becomes significant. In 2003, Yerworth *et al.* [17] presented a multifrequency EIT design named the Sheffield Mark 3.5 which provided up to 64 electrodes for imaging in the head. It was operated at a frequency selectable from 18 frequencies between 225Hz and 77kHz and was employed in clinical trials of multifrequency EIT in stroke, epilepsy, and neonatal brain injury. In 2014, Wi *et al.* [18] proposed a MFEIT system called the KHU Mark 2.5. The system can maintain a signal-to-noise ratio (SNR) of 80 dB for the frequency up to 250 kHz and a reciprocity error below 0.5% over continuous operation for 24 hours. In 2016, Santos *et al.* [19] developed a new prototype of the MFEIT system utilizing a composite waveform as the excitation signal to show preliminary frequency-difference images of in-vivo experiments. In 2017, Yang *et al.* [20] developed a MFEIT system with demi-parallel structure for real-time 2-D and 3-D imaging. The system achieved a high frame rate of up to 1014 frame/s and a high SNR of up to 82.28 dB over 1kHz-1MHz. In 2019, Wu *et al.* [21] developed a highly integrated wearable MFEIT system, which used 16 new active electrodes and had a frame rate of 122 frames/s with a wide bandwidth of 1MHz. In 2020, Allegri *et al.* [22] presented a monolithic microsystem that can perform bio-impedance analysis and EIT measurements as well as record electrocardiogram signals. The tuning range of the system was from 10kHz to 10MHz and the common-mode rejection ratio was 81 dB at 10kHz, which increased to 84 dB at 10MHz. In 2021, Xu *et al.* [23] designed an FPGA-based MFEIT system where precise amplitude and phase measurement can be implemented. The maximum SNRs of the amplitude and phase

measurement are 71.55 dB and 64.12 dB, respectively. These efforts and progresses show the potential of multifrequency measurement and lay the foundation for further development of MFEIT. However, few types of research on the multifrequency CCEIT (MFCCEIT) system have been reported. Research work on the MFCCEIT system should be undertaken to further exploit the potential of CCEIT in biomedical applications.

This work presents the development of an MFCCEIT system with a wide bandwidth. It is developed from the aspects of the MFCCEIT system (hardware), the impedance calculation model, and the system evaluation.

- 1) A new MFCCEIT system will be developed for multifrequency data acquisition and impedance measurement. The system consists of the 12-electrode CCEIT sensor, the sensing modules, the data acquisition module, and the personal computer (PC).

2) To implement accurate impedance measurement, an impedance calculation model will be established by combining mechanism modeling of the integrated circuits (ICs) and empirical modeling of the measurement data with the least squares (LS) method.

3) Experiments will be carried out to verify the effectiveness of the developed MFCCEIT system, including the SNR, the impedance measurement accuracy, and the imaging performance in biomedical applications.

The rest of this paper is organized as follows. Section II describes the overview of the MFCCEIT system. Section III and Section IV describe the design of the sensing module and the data acquisition module in the MFCCEIT system, respectively. Section V focuses on the establishment of the impedance measurement model. The evaluation of the system from multiple aspects and the experimental results are presented in section VI. Section VII gives the conclusion.

II. SYSTEM OVERVIEW

A. System Architecture

According to the previous research results, a relatively high frequency is recommended for CCEIT to ensure a high SNR of the impedance measurement and ensure good imaging performance [24]. And it is also indicated that CCEIT could have a larger excitation frequency domain than that of the traditional EIT [13, 14]. So, the MFCCEIT system is expected to obtain the bio-impedance in a large frequency domain. That means to ensure a good performance of the system, the IC

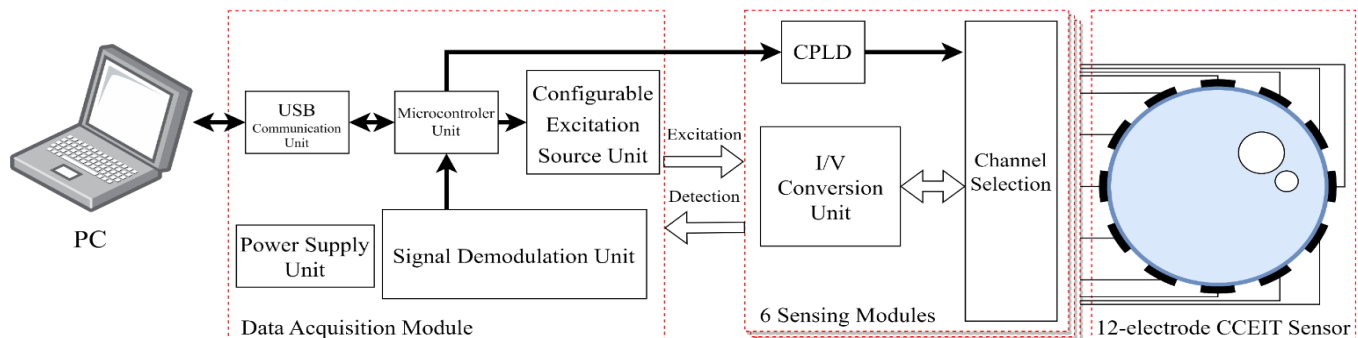


Fig. 1. Architecture of the MFCCEIT system.

selections should support the requirement of the frequency range and the circuit design needs to consider some factors such as signal crosstalk and impedance matching, especially at high working frequency. Based on these considerations, the basic architecture of the MFCCEIT system is designed, as shown in Fig.1. The designed system consists of a 12-electrode CCEIT sensor, 6 dual-channel sensing modules, a data acquisition module, and a personal computer (PC). The sensing module is used for channel selection and signal detection. The data acquisition module is designed to generate configurable multifrequency excitation signals and implement data acquisition of the detection signal and measurement of the impedance. The PC is used for image reconstruction.

B. The 12-electrode CCEIT Sensor

Fig.2 shows the construction of the 12-electrode CCEIT sensor, with 12 electrodes attached equidistantly to the outer surface of an insulating layer. In this way, the electrodes and the biological medium in the sensing area are not in direct contact and the contact impedance can be avoided. For each electrode, the electrode, the insulating layer, and the biological medium will form a coupling capacitance. CCEIT adopts the voltage excitation and current detection strategy. When a measurement electrode pair, including an excitation electrode and a detection electrode, is selected, the equivalent circuit of this electrode pair can be simplified as two coupling capacitances C_1 , C_2 in series with an impedance Z_x , as shown in Fig. 2. Here, Z_x is the equivalent impedance of the biological medium between the electrode pair. During the whole measurement cycle of CCEIT, the 1st electrode and the 2nd electrode are selected as the first electrode pair for impedance measurement, then the 1st electrode and the 3rd electrode, ..., till the 1st electrode and the 12th electrode, respectively. Then, the impedance between the 2nd electrode and the 3rd electrode, ..., till the 2nd electrode and the 12th electrode are measured by turn. Go on until the 11th electrode and the 12th electrode are selected as the electrode pair to obtain the impedance. Accordingly, 66 independent impedance measurement is realized in a measurement cycle by the 12-electrode CCEIT sensor, where a frame of 66 impedance values (including 66 real part values and 66 imaginary part values) can be further calculated for image reconstruction.

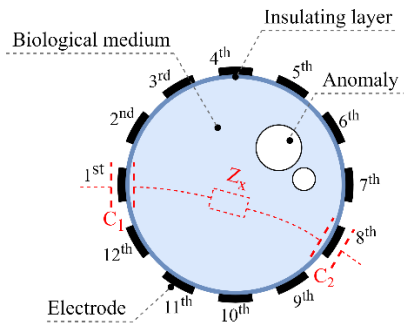


Fig. 2. Construction of sensor and the equivalent circuit.

III. THE SENSING MODULE

As mentioned, the sensing module is to implement channel

selection and signal detection, which mainly includes the selection and switch of the measurement electrode pair, and the current-to-voltage (I/V) conversion of the output current signal of the sensor. Therefore, three units, i.e. the I/V conversion unit, the channel selection unit, and the complex programmable logic device (CPLD), are designed. The CPLD is used to provide the control signal of the switching process. Each sensing module consists of two-channel selection units, which are responsible for the switch and selection of two adjacent electrodes. So, there are 6 dual-channel sensing modules in the system. Fig. 3 is the photo of the developed sensing module.

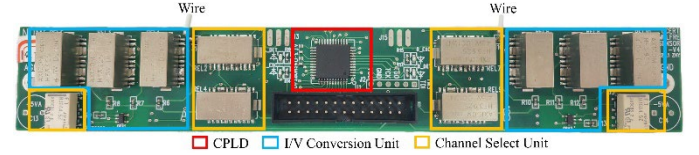


Fig. 3. Photo of the developed sensing module.

The I/V conversion unit

When an excitation voltage is applied to the excitation electrode, a current that reflects the impedance information of the biological medium will be obtained on the detection electrode. Then this current signal is converted to a voltage signal for subsequent impedance measurement. Here, an inverting amplifier circuit based on OPA659 is designed. The OPA659 is a unity-gain stable operational amplifier (AMP) that has a wide bandwidth of up to 650MHz when the gain is 1, and it also has the advantages of high input impedance, low bias current, and low integrated noise. The bandwidth of the AMP is determined by a constant index named gain bandwidth product (GBP), which is depicted as follows:

$$GBP = \text{Bandwidth} \times \text{Gain} \quad (1)$$

Equation (1) indicates that as the gain increases, the bandwidth of AMP narrows. For the MFCCEIT system, the target frequency range is large, which narrows the gain configured to the AMP. Besides, the biological medium has frequency dependence, i.e., the impedance decreases as the frequency goes up. That means the value of the impedance may cover a wide range as well. So, a suitable feedback resistance is particularly important to keep the gain of the AMP within a reasonable range to ensure high SNR and stable detection performance. Fig. 4 shows the I/V conversion unit, where a feedback path with three parallel feedback resistances R_{f1} , R_{f2} , and R_{f3} is designed. V_{in} is the exciting voltage applied to the excitation electrode and I_{out} is the output current obtained on the detection electrode. Here, Z_x is the interested impedance. V_{out} is the output voltage of the I/V conversion unit. The three feedback resistances can be freely selected and combined according to the frequency and the frequency characteristic of the interested bio-impedance. At low frequencies, where the impedance is expected to be larger, the larger feedback resistance will be connected to the feedback path. Conversely, at high frequency, the smaller feedback resistance will be switched to the feedback path. In this work, to take advantage of the unity-gain stable property of the AMP, R_{f1} , R_{f2} , and R_{f3} are respectively configured as 510 Ω , 1k Ω , and 5.1k Ω . The switch and combination of the three feedback resistances are

implemented by three high-frequency relays S_{f1} , S_{f2} , S_{f3} controlled by the CPLD (xc9572). To implement effective switching at the target wide frequency range, the single-pole double-throw relay HF353 is selected as the relay. The isolation characteristic of HF353 is -80dB at 1GHz, which ensures an outstanding isolation ability to avoid the coupling of the AC signals, especially the high-frequency signals.

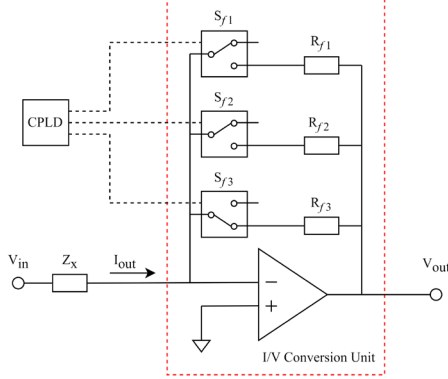


Fig. 4. The I/V conversion unit.

B The channel selection unit

There are 6 sensing modules in the designed system and each of them contains 2 channel selection units. To implement the switching of the electrodes, the 12 electrodes are connected to the 12 channel selection units, respectively. When a measurement electrode pair is selected, one electrode is switched to the excitation mode, the other electrode is switched to the detection mode. And the rest 10 electrodes are switched to idle mode. Therefore, three modes are designed for each electrode, including the excitation mode, the detection mode, and the idle mode. To implement effective switching at the target wide frequency range, the single-pole double-throw relays (HF353 and FTR-B3GA4.5Z) are selected as the switches. The isolation characteristic of HF353 is -80dB at 1GHz, which ensures an outstanding isolation ability to avoid the coupling of the AC signals, especially the high-frequency signals.

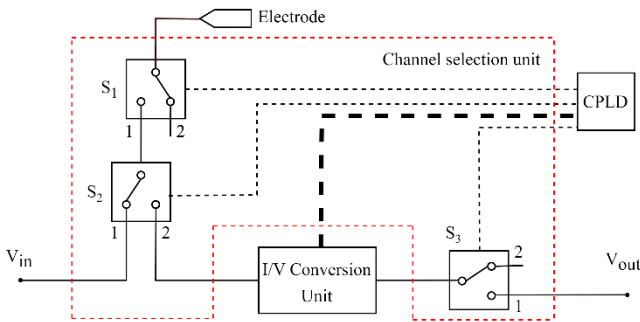


Fig. 5. The channel selection unit at the default idle mode.

Fig. 5 shows the basic construction of the channel selection unit connected to the electrode, which consists of three relays S_1 , S_2 , and S_3 controlled by the CPLD. The HF353 is selected for S_1 and S_2 , and the relay FTR-B3GA4.5Z is selected for S_3 . When the electrode is at the default idle mode, S_1 and S_3 are switched to port 2, and S_2 is switched to port 1. When the

electrode is selected as the excitation electrode, S_1 and S_2 are switched to port 1, while S_3 is switched to port 2. Then, the excitation signal V_{in} will be applied to this electrode. When the electrode is in the detection mode, S_1 and S_3 are switched to port 1, and S_2 is switched to port 2. Then the corresponding output signal (I_{out}) could be obtained on this electrode for subsequent detection and impedance measurement. Fig.6 illustrates an example of the channel selection of a measurement electrode pair (the 1st-2nd electrode pair) connected to two-channel selection units. In this example, the 1st electrode is in the excitation mode and the 2nd electrode is in the detection mode. The purple line represents the effective signal path of the selected electrode pair. The rest 3rd-12th electrodes are in idle mode, which is not illustrated in Fig. 6.

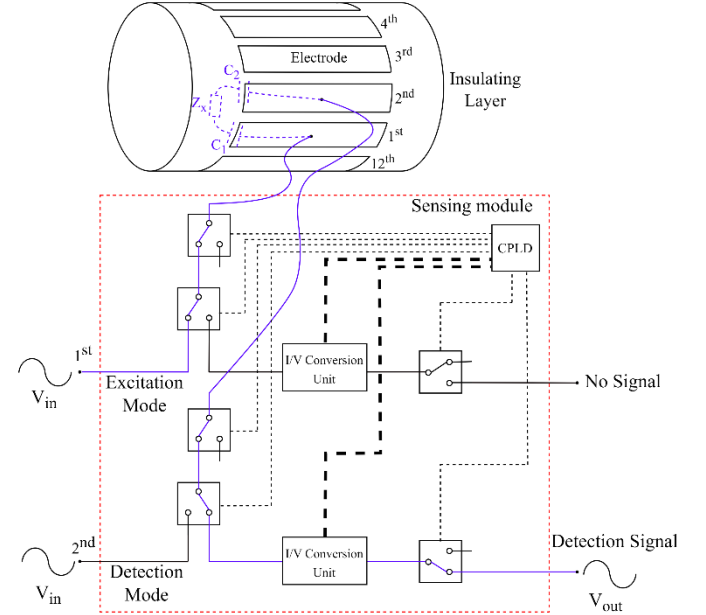


Fig. 6. An example of the channel selection of a measurement electrode pair (the 1st-2nd electrode pair). Phantom in vertical position? Horizontal is normally pipeline? Or just 2D like Fig. 2.

IV. THE DATA ACQUISITION MODULE

As shown in Fig.1, the data acquisition module is composed of the microcontroller unit (MCU), the configurable excitation source unit, the signal demodulation unit, the universal serial bus (USB) communication unit, and the power supply unit. Fig. 7 shows the detailed construction of the data acquisition module. The STM32F103, which has abundant peripherals to ensure good cooperation performance of the units in the system, is selected as the MCU to control the cooperative work between the units and implement the whole measurement process. The configurable excitation source consists of a wideband direct digital synthesizer (DDS) and a low pass filter (LPF) designed to generate stable and configurable excitation signals. The signal demodulation unit, which demodulates the detection signal obtained by the sensing module for impedance calculation, is designed based on a gain phase detector (GPD) and an analog-to-digital converter (ADC). The USB communication unit is constructed by a USB bus convert chip (CH340N). It sends the demodulated impedance data to PC for

image reconstruction. The power supply unit powers the ICs in the system. Fig.8 shows the photo of the developed data acquisition module.

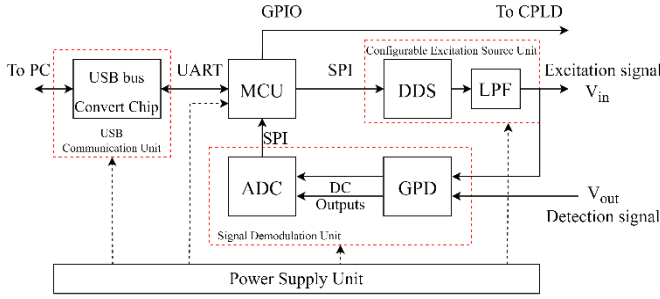


Fig.7. The detailed construction of the data acquisition module.

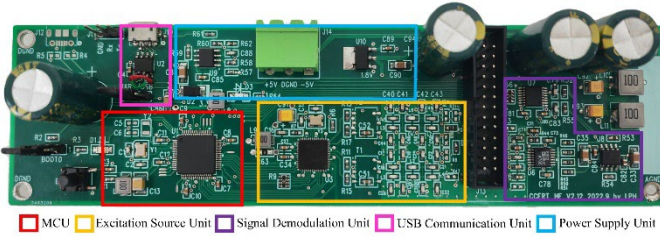


Fig. 8. The developed data acquisition module.

The generation of a reliable multifrequency excitation signal and the demodulation of the detection signal are the most critical parts of the data acquisition module. Therefore, the design of the configurable excitation source and the signal demodulation unit are described in detail.

1) Configurable Excitation Source

The excitation source of a multifrequency system should have a frequency adjustable and stable output over a wide frequency range with good load-carrying capability. In this system, a configurable DDS (AD9958) and a low-pass filter (LPF) are combined to develop the configurable excitation source. The AD9958 consists of two DDS cores that provide independent frequency, phase, and amplitude controls. It can generate a sinusoidal signal of a frequency of up to 250MHz. Moreover, it has the advantages of excellent frequency tuning resolution up to 0.12Hz and high-speed SPI with 800Mbps data throughput. The output frequency (f_{out}) of the DDS is a function of the rollover rate of each phase accumulator. The exact relationship is given as:

$$f_{out} = \frac{FTW \times f_{clk}}{2^{32}} \quad (2)$$

where f_{clk} is the system clock. FTW is the frequency tuning word and satisfies $0 \leq FTW \leq 2^{32}$, with 2^{32} representing the capacity of the phase accumulator. The AD9958 incorporates a 10-bit current output digital-to-analog converter (DAC) which can be modeled as a current source with high output impedance. For the convenience of subsequent impedance measurement, an equivalent transformation from the current source to the voltage source is introduced for the configurable excitation source.

2) Signal Demodulation Unit

To implement effective demodulation of the detection signal

in a wide bandwidth and simplify the system, the GPD is used in the proposed system. It can determine the magnitude ratio and phase difference between the excitation signal V_{in} from the configurable excitation source and the detection signal V_{out} from the sensing module. Here, a high-performance GPD (AD8302) with a wide bandwidth of up to 2.7 GHz is adopted. Fig.9 shows the basic construction of signal demodulation units, including the GPD and the ADC.

As shown in Fig.9, in GPD, a pair of matched logarithmic amplifiers (LOG AMPs) and a phase detector are used to obtain the gain and phase information of the two input signals (the excitation signal and the detection signal). The LOG AMP provides a logarithmic compression function that converts the input voltage signal to a compact decibel-scaled output. Since subtraction in the logarithmic domain corresponds to the ratio in the linear domain, the two outputs of the LOG AMPs are subtracted to obtain the amplitude output V_{MAG} , which is a DC voltage output corresponding to the magnitude ratio of the two input signals:

$$V_{MAG} = V_{SLP} 20 \log_{10} \left(\frac{|V_{INA}|}{|V_{INB}|} \right) = V_{SLP} 20 \log_{10} \left(\frac{|V_{out}|}{|V_{in}|} \right) \quad (3)$$

where V_{INA} and V_{INB} are the two input voltage signals, i.e. the excitation signal and the detection signal, respectively. V_{SLP} is the slope in mV/dB which is a fixed parameter of the LOG AMP. AD8302 has an accurate gain measurement scaling up to 30mV/dB. At the same time, the two outputs of the LOG AMPs drive an exclusive-OR style digital phase detector to obtain the phase output V_{PHS} , which is a DC voltage output corresponding to the phase difference of the two input signals:

$$V_{PHS} = V_{\phi} (\angle V_{INA} - \angle V_{INB}) = V_{\phi} (\angle V_{out} - \angle V_{in}) \quad (4)$$

where V_{ϕ} is the constant slope in mV/degree. AD8302 has an accurate phase measurement scaling up to 10mV/degree. $\angle V_{INA}$ and $\angle V_{INB}$ represent the phases of the two input signals in degrees, respectively.

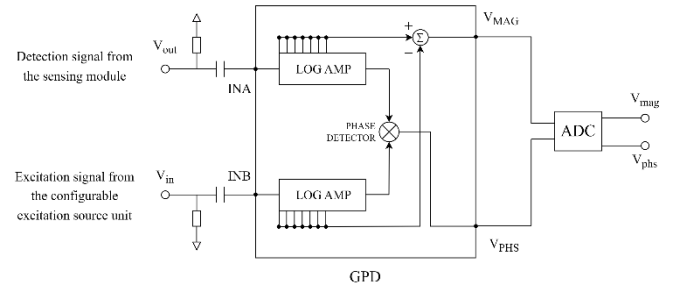


Fig. 9. The basic construction of the signal demodulation unit.

So, the V_{MAG} and the V_{PHS} obtained by the GPD reflect the difference in information between the excitation signal and the detection signal, which are determined by the interested impedance. After obtaining the two DC output voltage signals of GPD (V_{MAG} and V_{PHS}), a 16-bit ADC (ADS8328) with a sampling rate of 500kHz is employed to obtain the discretized values of the two output signals (V_{mag} and V_{phs}). Finally, with the V_{mag} and V_{phs} , the interested impedance (the real part and the imaginary part) can be calculated by establishing an impedance calculation model.

V. IMPEDANCE CALCULATION MODEL

The impedance calculation model reveals the relationship between the interested impedance (Z_x) and the outputs of the signal demodulation unit (V_{mag} and V_{phs}). Theoretically, this relationship can be deduced from the ratio between the input (the excitation signal) and the output (the detection signal) of the AMP, and the correlation between the input and the output of the GPD. However, the practical situation is non-ideal. On the one hand, the actual model deviates from the ideal model due to the limitation of the frequency characteristics of the ICs. On the other hand, the detection signal will be inevitably interfered with because of the non-perfect circuit design. In the proposed system, the key ICs to deal with the detection signal are the AMP and the GPD. So, the establishment of the impedance calculation model mainly depends on the analysis of the AMP and the GPD.

1) An ideal AMP is modeled as a voltage-controlled voltage source (VCVS), whose open-loop gain is infinite. Accordingly, the closed-loop gain of the I/V conversion unit A_{cl} is:

$$A_{cl} = \frac{V_{out}}{V_{in}} = -\frac{R_f}{Z_x} \quad (5)$$

where R_f is the feedback resistance and Z_x is the interested impedance to be measured. However, in the real case, the open-loop gain of the AMP has an upper cut-off frequency, which leads to the deviation of the output of the I/V conversion unit as the frequency increases. If (5) is used to calculate Z_x , considerable measurement error will be introduced at high frequency.

2) For the GPD, the output DC voltages (V_{mag} and V_{phs}) are ideally linear to the amplitude ratio (logarithmic) and the phase difference of the two input signals, respectively, as shown in (3) and (4). However, the interferences, such as signal crosstalk, stray capacitances, and wire inductances, will inevitably introduce deviations to the outputs of the GPD. In this case, measurement error of the impedance will also be introduced, and calibration is needed.

Based on the above analysis, the impedance calculation model is established by the modeling for the AMP and the modeling for the GPD, as shown in Fig. 10. For the AMP, mechanism modeling will be carried out to develop the relationship between the known impedance Z_x and the closed-loop gain of the I/V conversion unit A_{cl} , i.e., $A_{cl} = h_3(Z_x)$. For the GPD, empirical modeling will be undertaken to develop the correlation between V_{mag} and the amplitude of A_{cl} ($|A_{cl}|$), i.e., $|A_{cl}| = h_1(V_{mag})$, and the correlation between V_{phs} and the phase of the A_{cl} ($\angle A_{cl}$), i.e., $\angle A_{cl} = h_2(V_{phs})$, respectively. In this way, the model which reveals the relationship between the interested impedance Z_x and the outputs of the system (V_{mag} and V_{phs}) is established.

For practical impedance measurement, with the established impedance calculation model, the impedance measurement is a reverse process, as shown in Fig. 10. After the V_{mag} and the V_{phs} are obtained by the hardware, $h_1(V_{mag})$ and $h_2(V_{phs})$ will be applied first to calculate the amplitude and the phase of A_{cl} , respectively. Then, with the obtained A_{cl} , $g(A_{cl}) = h_3^{-1}(A_{cl})$

will be used to calculate the interested unknown impedance Z_x .

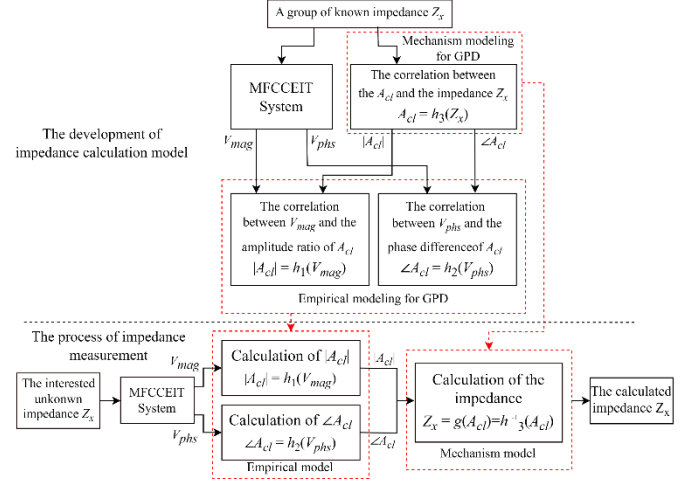


Fig.10. The development of the impedance calculation model and the process of impedance measurement.

A. Mechanism Modeling of the AMP

In the I/V conversion unit, the AMP is employed as a closed-loop system, as shown in Fig. 11(a). In this case, the open-loop input voltage of the AMP is $-V_-$ because V_+ is zero. And the V_- derives from two aspects, as shown in Fig. 11(b). One is the forward voltage V_f generated by the excitation signal V_{in} and the other is the backward voltage V_b generated by the detection signal V_{out} . The open-loop input voltage of the AMP is then calculated as:

$$V_+ - V_- = -V_- = -(V_f + V_b) \quad (6)$$

Fig. 12 depicts the closed-loop control system of the I/V conversion unit. In the figure, α is the feedforward factor corresponding to V_f and β is the feedback factor corresponding to V_b . They can be calculated by the interested impedance Z_x and the feedback resistance R_f as:

$$\alpha = \frac{V_f}{V_{in}} = \frac{R_f}{Z_x + R_f} \quad (7)$$

$$\beta = \frac{V_b}{V_{out}} = \frac{Z_x}{Z_x + R_f} \quad (8)$$

A_{ol} is the open-loop gain of the AMP, which is described as:

$$A_{ol} = \frac{A}{1 + j \frac{f}{f_c}} \quad (9)$$

where f is the frequency of the signal. f_c is the upper cut-off frequency of the AMP. It is approximate to the bandwidth of the AMP and can be calculated based on (1) as:

$$f_c \approx \text{Bandwidth} = \frac{GBP}{A} \quad (10)$$

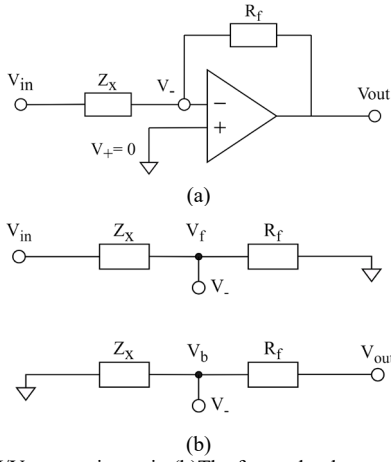


Fig. 11. (a) The I/V conversion unit. (b) The forward voltage and the backward voltage are based on the principle of voltage division.

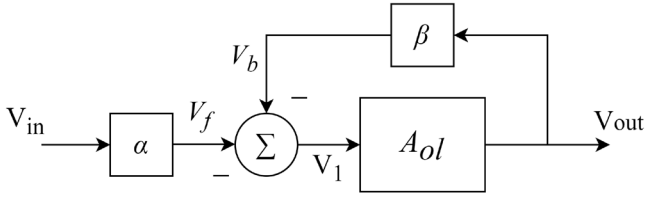


Fig. 12. The closed-loop control system of the I/V conversion unit.

Based on Fig. 12, the closed-loop gain A_{cl} of the I/V conversion unit is derived as:

$$A_{cl} = \frac{V_{out}}{V_{in}} = -\alpha \frac{A_{ol}}{1 + \beta A_{ol}} \quad (11)$$

So, according to (7)-(11), the relationship between Z_x and A_{cl} can be described as:

$$A_{cl} = h_3(Z_x) = \frac{-R_f A_f c}{f_c(Z_x + R_f + Z_x A) + jf(Z_x + R_f)} \quad (12)$$

$$Z_x = g(A_{cl}) = h_3^{-1}(A_{cl}) = \frac{-R_f[GBP(A + A_{cl}) + jfA \cdot A_{cl}]}{A_{cl}[GBP(1 + A) + jfA]} \quad (13)$$

where the GBP and A are the known characteristics of the AMP. At the specified frequency f , the R_f is a determined feedback resistance. Therefore, with (12) and (13), A_{cl} and Z_x can be uniquely determined by each other.

B. Empirical Modeling for the GPD

The amplitude (logarithmic) and phase of A_{cl} can be written as:

$$|A_{cl}| = 20 \log_{10} \frac{|V_{out}|}{|V_{in}|} \quad (14)$$

$$\angle A_{cl} = \angle V_{out} - \angle V_{in} \quad (15)$$

According to (3), (4), (14), (15), the relationships between the two output DC voltages of GPD (V_{mag} and V_{phs}) and the closed-loop gain of the I/V conversion unit A_{cl} ($|A_{cl}|$ and $\angle A_{cl}$) are clear. However, as mentioned, the outputs of the GPD are usually non-ideal because of the interferences in the real case, which will result in the deviation of the impedance measurement. So, empirical modeling is introduced to calibrate

the relationships, which is to establish the correlation model between V_{mag} and $|A_{cl}|$, and the correlation model between V_{phs} and $\angle A_{cl}$.

To investigate the correlations, pre-experiments were carried out. Fig. 13 shows the corresponding results, where the ideal correlation and the practical correlations at 3 different test frequencies are displayed. The results indicate the necessity of calibration and show that the correlations have obvious linear properties. Therefore, linear calibration is introduced to develop the models, which can be represented as:

$$|A_{cl}| = h_1(V_{mag}) = k_1 V_{mag} + b_1 \quad (16)$$

$$\angle A_{cl} = h_2(V_{phs}) = k_2 V_{phs} + b_2 \quad (17)$$

where k_1 and k_2 are the slopes and b_1 and b_2 are the intercepts of the two correlation models, respectively.

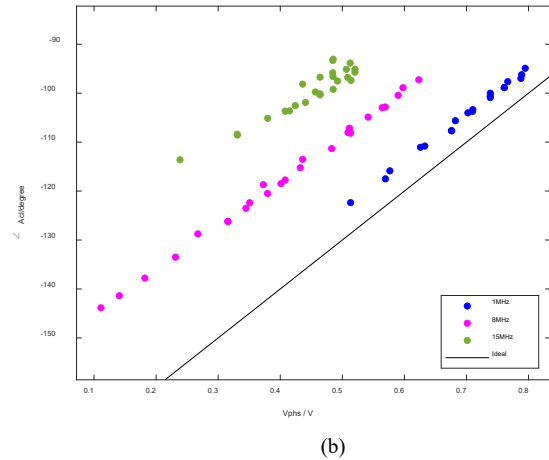
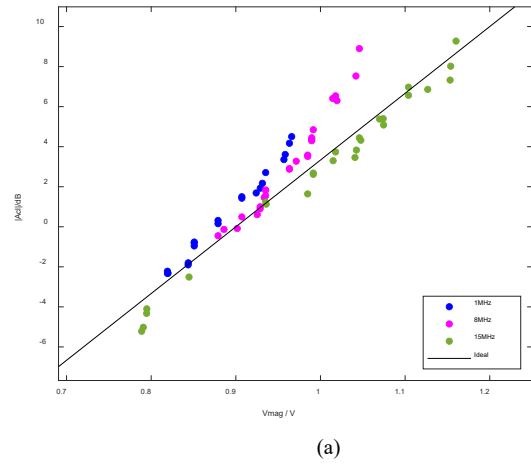


Fig. 13. Results of pre-experiments: (a) The correlation between the $|A_{cl}|$ and the V_{mag} . (b) The correlation between the $\angle A_{cl}$ and the V_{phs} .

The empirical modeling for the GPD includes 3 steps:

1) For each frequency point, a series of resistor-capacitor combinations with known Z_x are selected and the corresponding theoretical A_{cl} is calculated according to (13) for each resistor-capacitor combination. To establish a reasonable empirical model, the frequency-dependence characteristic of the biological medium is taken into consideration. The resistor-capacitor combinations at different frequencies are selected

according to the spectroscopy impedance of the phantom developed with different materials measured by the impedance analyzer (Keysight E4294A).

2) For each resistor-capacitor combination, the corresponding outputs of the signal demodulation unit (V_{mag} and V_{phs}) at different frequencies are obtained by the MFCCEIT system.

3) For each frequency point, linear fitting based on the LS method with the models (16), (17) is carried out to determine the parameters (the slopes k_1 , k_2 , and the intercepts b_1 , b_2) of the two correlation models.

Fig.14 depicts the established empirical models h_1 and h_2 (the solid lines) at different frequencies. Fig.14(a) shows the models h_1 between the V_{mag} and the $|A_{cl}|$ at different frequency points. Fig.14(b) shows the models h_2 between the V_{phs} and the $\angle A_{cl}$ at the listed frequency points.

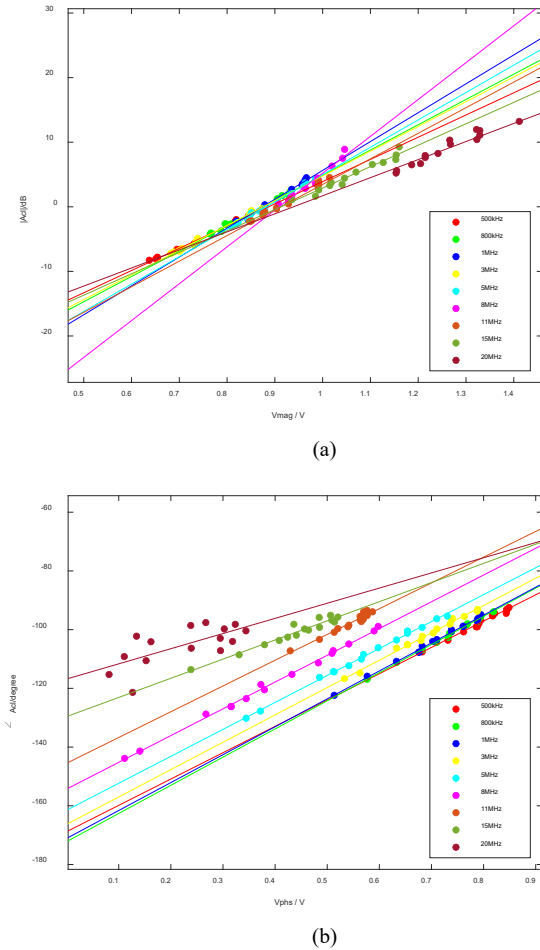


Fig. 14. Empirical models for GPD at different frequencies: (a) The models between v_{mag} and $|A_{cl}|$. (b) The models between v_{phs} and $\angle A_{cl}$.

VI. SYSTEM EVALUATION

In this section, the developed MFCCEIT system is evaluated from the aspects of signal-to-noise ratio (SNR) and impedance measurement accuracy.

A. Signal-to-Noise Ratio

SNR is an important index that evaluates the signal quality of the system [25]. A general definition of SNR can be

described as:

$$SNR = 10 \lg \frac{\sum_{i=1}^n v_i^2}{\sum_{i=1}^n (v_i - \bar{v})^2} \quad (18)$$

where n is the number of measurements of the signal v used for the calculation of SNR. v_i is the i^{th} measurement of the signal. \bar{v} is the mean value of the n measurements. Here, n is set to 100.

Here, the oscilloscope is used to sample the detection signal (V_{out}), i.e., the output of the I/V conversion unit and the input of the GPD, and the corresponding SNRs at different frequencies are calculated according to (18). For the 12-electrode CCEIT sensor, 66 SNRs are calculated to evaluate the performance of different electrode pairs. Fig.15 illustrates the SNRs of the system at 1MHz, 5MHz, 10MHz, 15MHz, and 20MHz, respectively. Table I shows the average value of the 66 SNRs at each frequency. It is indicated that like the conventional EIT systems, as the frequency increases, the SNR of the MFCCEIT also shows an overall downward trend. The average SNRs of the detection signal at 1MHz and 20MHz are 86.04dB and 65.00dB, respectively.

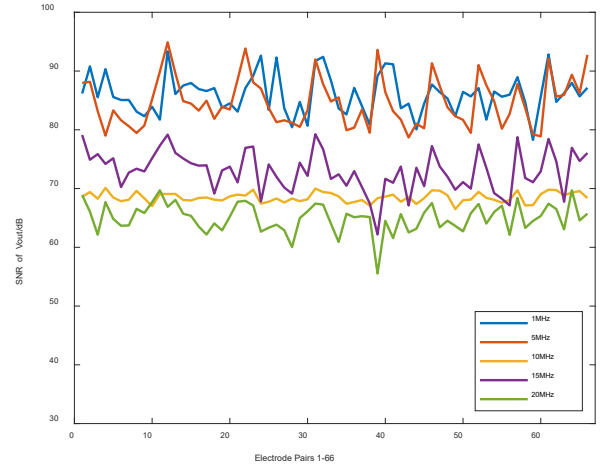


Fig. 15. The SNR of the system at different frequencies.

TABLE I AVERAGE SNR OF THE SYSTEM AT DIFFERENT FREQUENCIES					
Frequency (MHz)	1	5	10	15	20
SNR (dB)	86.04	84.72	68.49	72.99	65.00

B. Impedance Measurement Accuracy

To evaluate the impedance measurement performance of the CCEIT system, several resistor-capacitor combinations, are used to test the developed system. These resistor-capacitor combinations are also selected according to the frequency-dependence characteristic of the biological medium but are different from those used in the development of the impedance measurement model. The impedance values at different frequencies measured by the system are compared with those measured by the impedance analyzer. The relative error (RE) of the impedance measurement is introduced, which can be described as:

$$RE = \frac{|Z_s - Z_l|}{Z_l} \times 100\% \quad (19)$$

where Z_S is the impedance measurement (real part or imaginary part) obtained by the developed system. Z_I is the impedance measurement obtained by the impedance analyzer. Table II shows the relative errors of the impedance measurement, where R means the nominal value of the resistor and C means the nominal value of the capacitor. As shown in Table II, it is found that the developed system has good impedance measurement accuracy at frequencies below 10 MHz, especially at frequencies below 5 MHz. For the test resistor-capacitor combinations, the maximum relative errors of the impedance measurement at different frequencies below 5 MHz and below

10 MHz are smaller than 9.13% and 16.44%, respectively. However, at frequencies higher than 10MHz, especially those higher than 15 MHz, the relative errors of impedance measurement are relatively large. The reason is that the tested impedance is smaller at higher frequencies, leading to a larger relative error in the impedance measurement. The maximum relative errors of the impedance measurement at 10MHz-20MHz for the real part and the imaginary part are 51.15% and 40.71%, respectively. The corresponding maximum absolute error of the impedance measurement is 57.95 Ω for the real part and 153.95 Ω for the imaginary part.

TABLE II
THE RELATIVE ERRORS OF THE IMPEDANCE MEASUREMENT

f	$R=0.51k\Omega$ $C=39pf$		$R=1k\Omega$ $C=39pf$		$R=1.5k\Omega$ $C=39pf$		$R=2k\Omega$ $C=39pf$		Mean error	
	Real	Imaginary	Real	Imaginary	Real	Imaginary	Real	Imaginary	Real	Imaginary
500kHz	9.36%	3.95%	11.76%	0.21%	1.16%	2.96%	5.49%	4.11%	6.94%	2.81%
800kHz	2.99%	1.23%	7.33%	3.72%	0.65%	0.22%	2.67%	0.71%	3.41%	1.47%
1MHz	4.21%	4.86%	0.35%	0.08%	3.85%	6.63%	2.42%	0.38%	2.71%	2.99%
2MHz	3.52%	2.29%	4.31%	9.09%	1.73%	1.18%	6.41%	3.33%	3.99%	3.97%
f	$R=200\Omega$ $C=39pf$		$R=300\Omega$ $C=39pf$		$R=470\Omega$ $C=39pf$		$R=510\Omega$ $C=39pf$		Mean error	
	Real	Imaginary	Real	Imaginary	Real	Imaginary	Real	Imaginary	Real	Imaginary
3MHz	7.99%	6.73%	1.81%	1.64%	4.18%	0.64%	3.72%	0.08%	4.43%	2.27%
5MHz	4.41%	0.84%	5.73%	8.90%	0.29%	2.56%	2.71%	5.23%	3.29%	4.38%
8MHz	2.55%	4.86%	3.02%	3.78%	7.90%	7.66%	15.60%	16.42%	7.27%	8.18%
f	$R=30\Omega$ $C=30pf$		$R=51\Omega$ $C=30pf$		$R=75\Omega$ $C=30pf$		$R=100\Omega$ $C=30pf$		Mean error	
	Real	Imaginary	Real	Imaginary	Real	Imaginary	Real	Imaginary	Real	Imaginary
10MHz	2.82%	5.46%	12.33%	17.89%	1.42%	2.88%	16.16%	21.34%	8.18%	11.89%
13MHz	1.19%	16.78%	16.81%	16.19%	22.56%	18.51%	14.17%	18.01%	13.68%	17.37%
15MHz	22.93%	26.75%	29.07%	19.53%	28.41%	20.87%	28.62%	27.85%	27.26%	23.75%
18MHz	44.18%	38.76%	49.52%	30.43%	41.06%	27.75%	42.69%	40.94%	44.36%	34.47%
20MHz	47.48%	45.33%	52.51%	38.03%	45.76%	35.40%	58.86%	44.07%	51.15%	40.71%

VII. IMAGE RECONSTRUCTION RESULTS

Image reconstruction experiments were carried out to verify the effectiveness of the MFCCEIT system. In the 12-electrode CCEIT sensor, the insulating layer was made of resin, which was fabricated by 3D printing. The outer diameter and thickness of the insulating layer were 160mm and 2mm, respectively. The 12 electrodes were made of a flexible printed circuit. The size of the electrodes was 34.9mm \times 60.0mm. Fig.17 shows five test distributions D1-D5 in the experiments. Water with the conductivity of $\sigma_1 = 0.012S/m$ and the relative permittivity of $\epsilon_1 = 78$ was used to simulate the background. Two kinds of materials, the non-conductive plastic rods, and the carrot sample, were used to simulate the anomalies and the \emptyset means of the diameter of the plastic rods/carrots.

To evaluate the imaging performance of the system, the classic linear back projection (LBP) algorithm is used to realize image reconstruction. The image correlation coefficient (ICC) is introduced as the quantitative index, which is defined as:

$$ICC = \frac{\sum_{i=1}^n (\tilde{g}_i - \tilde{g}_a)(g_i^* - g_a^*)}{\sqrt{\sum_{i=1}^n (\tilde{g}_i - \tilde{g}_a)^2 \sum_{i=1}^n (g_i^* - g_a^*)^2}} \quad (20)$$

where \tilde{g}_i is the i^{th} gray value in the normalized reconstructed image and g_i^* is the i^{th} gray value in the actual binary image of the tested distribution. \tilde{g}_a is the average gray value of the reconstructed image and g_a^* is the average gray value of the actual image. Table III shows the imaging results and the

corresponding ICC values. The results verified the effectiveness of the developed system. The reconstructed images based on either the real part or the imaginary part are consistent with the actual distributions at different frequencies. Besides, the MFCCEIT system can reconstruct the distributions with multiple anomalies or with different materials.

Fig. 17 The setups of the five distributions in the imaging experiment.

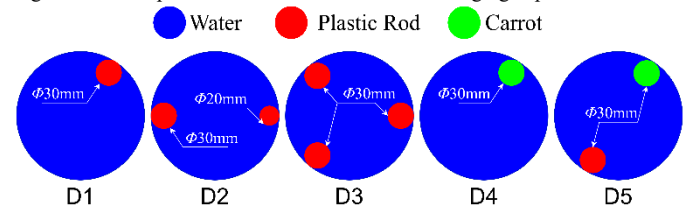
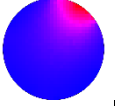





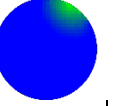
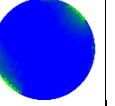
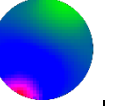
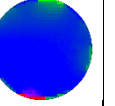




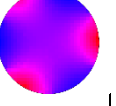

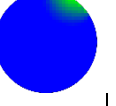
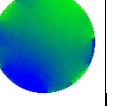
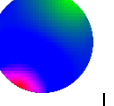
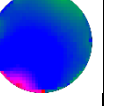


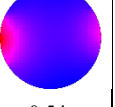
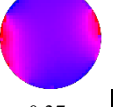

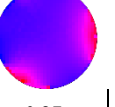
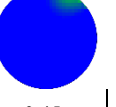
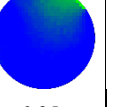
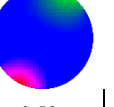
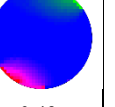
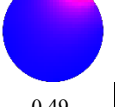
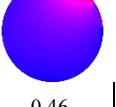


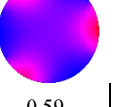

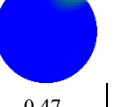
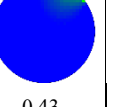
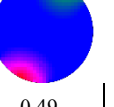
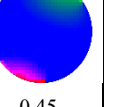
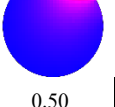
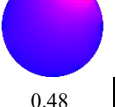
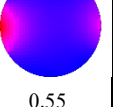
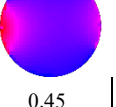

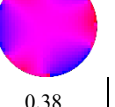
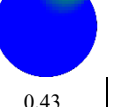
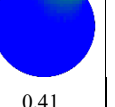
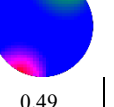
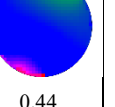
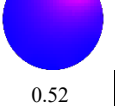
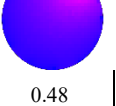
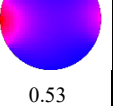
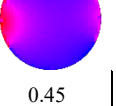
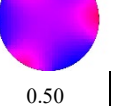
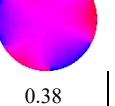
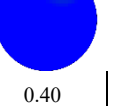
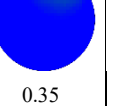
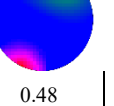
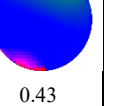
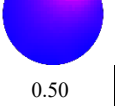
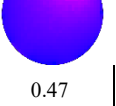
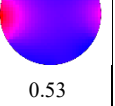
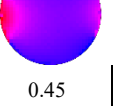
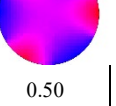
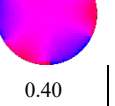
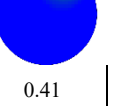
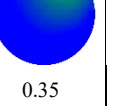
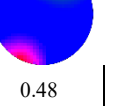
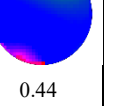
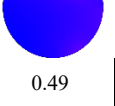

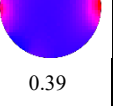
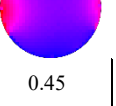
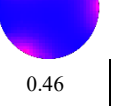
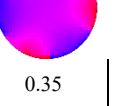
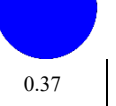
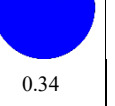
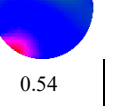
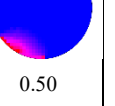
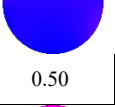
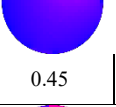
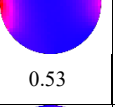
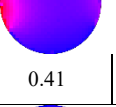
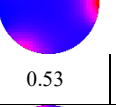
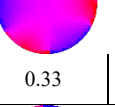
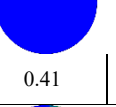
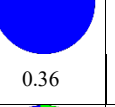
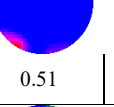
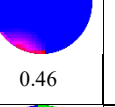
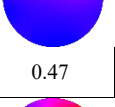
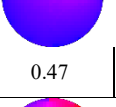
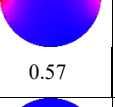
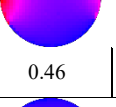
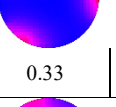
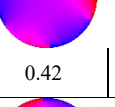
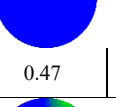
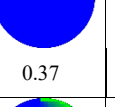
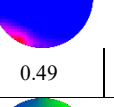
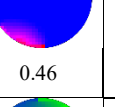
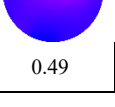
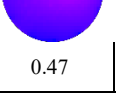
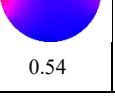
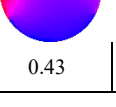
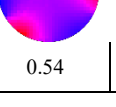
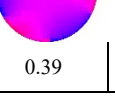
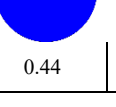
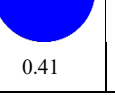
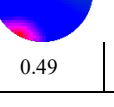
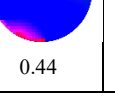


Fig. 17 The setups of the five distributions in the imaging experiment.

TABLE III
THE IMAGING RESULTS

	D1		D2		D3		D4		D5		
	Real	Imaginary	Real	Imaginary	Real	Imaginary	Real	Imaginary	Real	Imaginary	
500 kHz											
ICC	0.53	0.49	0.54	0.27	0.47	0.10	0.44	0.28	0.48	0.17	
800 kHz											
ICC	0.50	0.48	0.52	0.39	0.54	0.40	0.46	0.24	0.50	0.45	
1 MHz											
ICC	0.51	0.47	0.54	0.37	0.50	0.27	0.45	0.35	0.50	0.49	
3 MHz											
ICC	0.49	0.46	0.56	0.45	0.59	0.41	0.47	0.43	0.49	0.45	
5 MHz											
ICC	0.50	0.48	0.55	0.45	0.52	0.38	0.43	0.41	0.49	0.44	
8 MHz											
ICC	0.52	0.48	0.53	0.45	0.50	0.38	0.40	0.35	0.48	0.43	
10 MHz											
ICC	0.50	0.47	0.53	0.45	0.50	0.40	0.41	0.35	0.48	0.44	
13 MHz											
ICC	0.49	0.49	0.39	0.45	0.46	0.35	0.37	0.34	0.54	0.50	
15 MHz											
ICC	0.50	0.45	0.53	0.41	0.53	0.33	0.41	0.36	0.51	0.46	
18 MHz											
ICC	0.47	0.47	0.57	0.46	0.33	0.42	0.47	0.37	0.49	0.46	
20 MHz											
ICC	0.49	0.47	0.54	0.43	0.54	0.39	0.44	0.41	0.49	0.44	

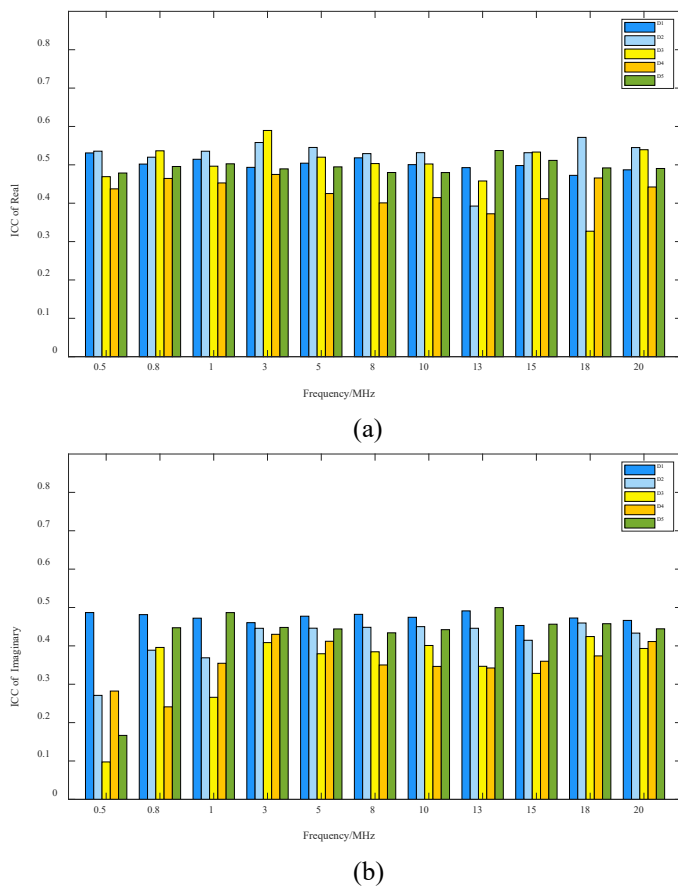


Fig. 18 The ICC of reconstructing D1-D5 both in the real part and imaginary part: (a) In the real part. (b) In the imaginary part.

VIII. CONCLUSION

In this work, an MFCCEIT system with a wide bandwidth of 20 MHz is developed. The system includes a 12-electrode CCEIT sensor, six sensing modules, a data acquisition module, and a personal computer (PC). An impedance calculation model, which combines the mechanism modeling of the integrated circuits (ICs) and the empirical modeling of the measurement data, is established. Experiments were carried out to verify the effectiveness of the MFCCEIT system. With proposed hardware system we evaluated the SNR, the impedance measurement accuracy, and the imaging performance at different frequencies. It is indicated that the development of the system is successful for potential biomedical application. The imaging results show that the system has good performance in the multifrequency imaging of multiple anomalies and multiple materials.

CCEIT overcomes the problems of contact measurement and insufficient usage of impedance, which is a promising contactless alternative to EIT in the biomedical field. However, as a new technique, the research on biomedical CCEIT is very limited. There is no targeted research on specific CCEIT systems for biomedical imaging. This work can provide new experiences and useful references for the further development of biomedical CCEIT. By taking advantage of multifrequency measurement acquisition of the complete impedance (both the real part and the imaginary part), the MFCCEIT system applies

to both time-difference and frequency-difference imaging and is expected to have wider application potential in our future studies.

REFERENCES

- [1] M. Wang, *Industrial Tomography: Systems and Applications*. Sawston, U.K.: Woodhead Publishing, 2015.
- [2] D. S. Holder, *Electrical Impedance Tomography: Methods, History, and Applications*. Bristol, U.K.: IOP Publishing, 2005.
- [3] R. J. Macdonald and E. Barsoukov, *Impedance Spectroscopy: Theory, Experiment, and Applications*. Hoboken, NJ, USA: Wiley, 2005.
- [4] L. Borcea, "Electrical impedance tomography," *Inverse Problems*, vol. 19, no. 4, p. 997, Jul. 2003.
- [5] M. Bodenstein, M. David, and K. Markstaller, "Principles of electrical impedance tomography and its clinical application," *Critical Care Medicine*, vol. 37, no. 2, pp. 713–724, Feb. 2009.
- [6] A. McEwan, G. Cusick, and D. S. Holder, "A review of errors in multi-frequency EIT instrumentation," *Physiol. Meas.*, vol. 28, no. 7, p. S197, Jun. 2007.
- [7] R. Cardu, P. H. W. Leong, C. T. Jin, and A. McEwan, "Electrode contact impedance sensitivity to variations in geometry," *Physiol. Meas.*, vol. 33, no. 5, pp. 817–830, May 2012.
- [8] T. Vilhunen, J. P. Kaipio, P. J. Vauhkonen, T. Savolainen, and M. Vauhkonen, "Simultaneous reconstruction of electrode contact impedances and internal electrical properties: I. Theory," *Meas. Sci. Technol.*, vol. 13, no. 12, pp. 1848–1854, Dec. 2002.
- [9] P. Hua, E. J. Woo, J. G. Webster, and W. J. Tompkins, "Finite element modeling of electrode-skin contact impedance in electrical impedance tomography," *IEEE Trans. Biomed. Eng.*, vol. 40, no. 4, pp. 335–343, Apr. 1993.
- [10] V. Kolehmainen, M. Lassas, and P. Ola, "Electrical Impedance Tomography Problem With Inaccurately Known Boundary and Contact Impedances," *IEEE Transactions on Medical Imaging*, vol. 27, no. 10, pp. 1404–1414, Oct. 2008.
- [11] Y. Wang, B. Wang, Z. Huang, H. Ji, and H. Li, "New capacitively coupled electrical resistance tomography (CCERT) system," *Meas. Sci. Technol.*, vol. 29, no. 10, p. 104007, Oct. 2018.
- [12] Y. Wang, H. Ji, Z. Huang, B. Wang, and H. Li, "Study on image reconstruction of capacitively coupled electrical impedance tomography (CCEIT)," *Meas. Sci. Technol.*, vol. 30, no. 9, p. 094002, Sep. 2019.
- [13] Y. Jiang and M. Soleimani, "Capacitively Coupled Resistivity Imaging for Biomaterial and Biomedical Applications," *IEEE Access*, vol. 6, pp. 27069–27079, 2018.
- [14] Y. D. Jiang and M. Soleimani, "Capacitively Coupled Electrical Impedance Tomography for Brain Imaging," *IEEE Trans. Med. Imaging*, vol. 38, no. 9, pp. 2104–2113, Sep. 2019.
- [15] X. He, Y. Jiang, B. Wang, H. Ji, and Z. Huang, "An Image Reconstruction Method of Capacitively Coupled Electrical Impedance Tomography (CCEIT) Based on DBSCAN and Image Fusion," *IEEE Trans. Instrum. Meas.*, vol. 70, pp. 1–11, 2021.
- [16] X. Bai, D. Liu, J. Wei, X. Bai, S. Sun, and W. Tian, "Simultaneous Imaging of Bio- and Non-Conductive Targets by Combining Frequency and Time Difference Imaging Methods in Electrical Impedance Tomography," *Biosensors*, vol. 11, no. 6, Art. no. 6, Jun. 2021.
- [17] R. J. Yerworth, R. H. Bayford, B. Brown, P. Milnes, M. Conway, and D. S. Holder, "Electrical impedance tomography spectroscopy (EITS) for human head imaging," *Physiol. Meas.*, vol. 24, no. 2, pp. 477–489, May 2003.
- [18] Hun Wi, H. Sohal, A. L. McEwan, Eung Je Woo, and Tong In Oh, "Multi-Frequency Electrical Impedance Tomography System With Automatic Self-Calibration for Long-Term Monitoring," *IEEE Trans. Biomed. Circuits Syst.*, vol. 8, no. 1, pp. 119–128, Feb. 2014.
- [19] S. Aguiar Santos, A. Robens, A. Boehm, S. Leonhardt, and D. Teichmann, "System Description and First Application of an FPGA-Based Simultaneous Multi-Frequency Electrical Impedance Tomography," *Sensors*, vol. 16, no. 8, p. 1158, Jul. 2016.
- [20] Y. Yang and J. Jia, "A multi-frequency electrical impedance tomography system for real-time 2D and 3D imaging," *Review of Scientific Instruments*, vol. 88, no. 8, p. 085110, Aug. 2017.
- [21] Y. Wu, D. Jiang, A. Bardill, R. Bayford, and A. Demosthenous, "A 122 fps, 1 MHz Bandwidth Multi-Frequency Wearable EIT Belt Featuring Novel Active Electrode Architecture for Neonatal Thorax Vital Sign

- Monitoring,” *IEEE Transactions on Biomedical Circuits and Systems*, vol. 13, no. 5, pp. 927–937, Oct. 2019.
- [22] D. Allegri, A. Donida, P. Malcovati, and D. Barrettino, “CMOS-Based Multifrequency Impedance Analyzer for Biomedical Applications,” *IEEE Trans. Biomed. Circuits Syst.*, vol. 12, no. 6, pp. 1301–1312, Dec. 2018.
- [23] Y. Xu, Z. Yan, B. Han, and F. Dong, “An FPGA-Based Multifrequency EIT System With Reference Signal Measurement,” *IEEE Trans. Instrum. Meas.*, vol. 70, pp. 1–10, 2021.
- [24] R. J. Halter, A. Hartov, and K. D. Paulsen, “A Broadband High-Frequency Electrical Impedance Tomography System for Breast Imaging,” *IEEE Trans. Biomed. Eng.*, vol. 55, no. 2, pp. 650–659, Feb. 2008.
- [25] S. Khan, P. Manwaring, A. Borsic, and R. Halter, “FPGA-Based Voltage and Current Dual Drive System for High Frame Rate Electrical Impedance Tomography,” *IEEE Trans. Med. Imaging*, vol. 34, no. 4, pp. 888–901, Apr. 2015.